

# Hexagonal Boron Nitride: Physical Properties, Hydride Vapor-Phase Epitaxy Growth of Large-Diameter Quasi-Bulk Wafers and Applications

Hongxing Jiang\* and Jingyu Lin\*

Hexagonal boron nitride (*h*-BN), with its ultrawide bandgap and 2D structure, holds an immense promise for advanced semiconductor applications. Scaling bulk crystals to large-diameter wafers, crucial for complex device fabrication, remains a challenge with high temperature, high pressure, and metal flux solution methods. To address this, recent efforts have focused on hydride vapor-phase epitaxy (HVPE) for producing large diameter thick *h*-BN quasi-bulk wafers, reaching hundreds of micrometers. These HVPE-grown quasi-bulk crystals exhibit excellent *c*-axis long-range order. Notably, the in-plane mobility-lifetime products for both electrons and holes surpass  $10^{-4} \text{ cm}^2 \text{ V}^{-1}$ , which are two orders of magnitude greater than the out-of-plane (vertical) values, highlighting the potential for high-performance devices leveraging superior lateral transport. Lateral detectors fabricated from 100  $\mu\text{m}$  thick B-10 enriched *h*-BN wafers have achieved a record 60% thermal neutron detection efficiency. Based on its physical properties, *h*-BN appears to be an outstanding material of choice for light-triggered electronic power switches capable of supporting high-voltage and high-power operations. These recent advancements in large-diameter *h*-BN quasi-bulk crystal growth, enabled by HVPE, pave the way for applications spanning deep UV photonics, high-power electronics, high-efficiency neutron detection, and quantum information technologies, establishing *h*-BN as both a versatile active semiconductor and an ideal substrate.

## 1. Introduction

It is well established that the performance metrics of semiconductor electronic devices exhibit a highly nonlinear relationship with the material's bandgap ( $E_g$ ). III-nitride wide bandgap (WBG) semiconductor light-emitting diodes (LEDs) and power electronic devices have revolutionized the energy sector by providing brighter, more energy-efficient, and reliable lighting solutions, as well as advanced power conversion systems.<sup>[1–9]</sup> These innovations have significantly reduced energy consumption and environmental impact.

H. Jiang, J. Lin  
Department of Electrical and Computer Engineering  
Texas Tech University  
Lubbock, TX 79409, USA  
E-mail: hx.jiang@ttu.edu; jingyu.lin@ttu.edu

 The ORCID identification number(s) for the author(s) of this article can be found under <https://doi.org/10.1002/pssb.202400605>.

DOI: 10.1002/pssb.202400605

The authors' invention of III-nitride microLED technology over 20 years ago<sup>[10–14]</sup> has not only created the microLED display industry but also spurred extensive research into microLEDs for augmented reality, virtual reality, and 3D (AR/VR/3D) microdisplays, as well as for neural interface and optogenetics applications.<sup>[11–15]</sup> Moreover, high indium-content InGaN and aluminum-content AlGaN alloy-based photonic devices are driving advancements in full-spectrum solar energy conversion, sterilization, and UV curing technologies.<sup>[16–19]</sup>

The crystal growth technology and use of hexagonal boron nitride (*h*-BN) as an ultrawide bandgap (UWBG) semiconductor are much less developed compared to other III-nitride materials. Moreover, *h*-BN is unique in terms of its crystalline structure. As illustrated in Figure 1a, *h*-BN has a layered crystalline structure and a close lattice match to graphite and hence to graphene, with the spacing between the stacked layers in the *c*-direction of 3.33 Å, giving a *c*-lattice constant of  $c = 6.66 \text{ \AA}$ . In Figure 1b, a cross-sectional view of transmission electron microscope (TEM) image

is shown for a freestanding *h*-BN quasi-bulk wafer of 100  $\mu\text{m}$  in thickness produced by hydride vapor-phase epitaxy (HVPE) by authors' group, which directly reveals that the spacing between the stacked planes in the *c* direction is 3.33 Å.<sup>[20]</sup> Because of its exceptional thermal and chemical stability, high thermal conductivity, outstanding electrical insulation characteristics, and strong resistance to oxidation and corrosion, *h*-BN has been extensively explored as an ideal material for use as a template, barrier, passivation layer, and gate material in the fabrication of novel 2D structures.<sup>[21]</sup> Additionally, *h*-BN serves as an effective host for optically stable single-photon emitters.<sup>[22]</sup>

In its 3D form, *h*-BN possesses extraordinary physical properties, including an UWBG of  $\approx 6 \text{ eV}$ <sup>[23–27]</sup> at room temperature, high breakdown field of  $\approx 12 \text{ MV cm}^{-1}$ ,<sup>[28,29]</sup> and high in-plane thermal conductivity of  $\approx 550 \text{ W m}^{-1} \text{ K}^{-1}$ .<sup>[30]</sup> Moreover, the isotope  $^{10}\text{B}$  in *h*-BN possesses an unusually large interaction cross section with thermal neutrons of  $\approx 3840$  barns ( $= 3.84 \times 10^{-21} \text{ cm}^2$ ).<sup>[31,32]</sup> The combination of these properties makes *h*-BN an outstanding UWBG material for diverse applications. Nevertheless, the bulk crystal growth techniques based on high-pressure and high-temperature (HPHT)<sup>[24,26–29]</sup> and metal

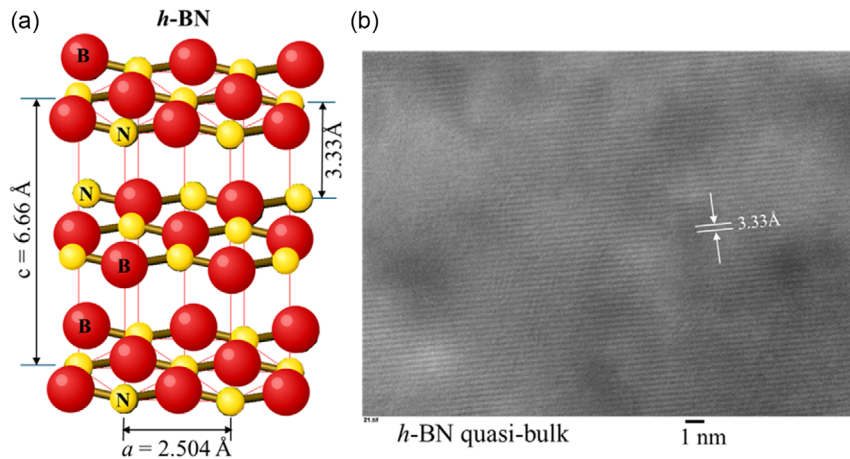


**Figure 1.** a) Schematic of crystalline structure of *h*-BN showing a *c*-lattice constant of  $c = 6.66 \text{ \AA}$  and spacing between stacked layers in the *c* direction of  $3.33 \text{ \AA}$ . b) Cross-sectional view of TEM image of a  $100 \mu\text{m}$  thick freestanding *h*-BN quasi-bulk wafer produced by HVPE, measuring a spacing of  $3.33 \text{ \AA}$  between the stacked layers in the *c* direction. Reproduced under terms of the CC-BY license.<sup>[20]</sup> Copyright 2024, The Authors.

flux solution methods<sup>[30]</sup> can only produce millimeter-size crystals with poor prospects of scaling up the wafer size. Therefore, the development of crystal growth technologies for producing large-diameter thick epitaxial films (or quasi-bulk wafers) is urgently needed.

We first discuss the recent advancements in understanding the detailed band-edge structure and fundamental properties of *h*-BN, which highlight *h*-BN's potential as an UWBG semiconductor for various applications. Following this, we provide an overview of recent developments in producing large-diameter *h*-BN quasi-bulk wafers, with diameters reaching up to 6 inches and thicknesses in the hundreds of micrometers, utilizing HVPE—a well-established technique for growing quasi-bulk AlN.<sup>[33,34]</sup> Furthermore, we present our demonstration of an active device that utilizes *h*-BN quasi-bulk crystals: high-efficiency thermal neutron detectors, the results of which will be discussed.

## 2. Basic Properties of *h*-BN

### 2.1. Energy Band Structure near Band Edge

Previous theoretical and experimental studies have revealed significant differences in the fundamental optical properties between *h*-BN<sup>[25,27,35–38]</sup> and wurtzite AlN.<sup>[39]</sup> All wurtzite III-nitrides (AlN, GaN, and InN) have direct bandgaps with the conduction band minimum (CBM) and valence band maximum (VBM) located at the  $\Gamma$  point.<sup>[39]</sup> Furthermore, energies at other high symmetry points in the first Brillouin zone (BZ), such as *L* and *K* points in wurtzite III-nitrides, are much higher than those at the  $\Gamma$  point. Consequently, the transport and optical properties of InN, GaN, and AlN, including the carrier effective masses and mobilities and band-edge optical transitions, are predominantly determined by the band parameters at the  $\Gamma$  point. **Figure 2a** shows the calculated band structure near the high symmetry *K* and *M* points in the first BZ of *h*-BN.<sup>[25,38]</sup> The results of the band structure calculations<sup>[25,38]</sup> and phonon-assisted photoluminescence (PL) measurements<sup>[27,40,41]</sup> have provided us with

the following insights concerning the band-edge structure of *h*-BN: 1) *h*-BN is an indirect gap semiconductor with a bandgap of around 6.0 eV at room temperature; 2) the CBM is at *M*-point and the VBM is at *K* point; and 3) the slope of the dispersion in the section between *M*-point and *K*-point (the *M*–*K* section) of the conduction band seems slightly larger than that of the valence band,<sup>[25,38]</sup> implying that the minimum direct energy bandgap of *h*-BN is at *M* point. The *M*–*K* section is thus most relevant for carrier generation under the above-bandgap photoexcitation and subsequent light emission.

Because of its indirect bandgap nature, direct band-to-band and excitonic transitions in *h*-BN are expected to be invisible or “dark”. **Figure 2b** shows a low-temperature phonon-assisted PL emission spectrum of a high-quality *h*-BN bulk sample with identification of the phonon modes<sup>[37]</sup> involved in the phonon-assisted recombination lines in *h*-BN and the scattering path in the first BZ with the green arrow corresponding to the phonon wavevector  $\mathbf{q} = \mathbf{KM}$ .<sup>[27]</sup> The indirect or “dark” exciton iX emission line appearing at 5.955 eV has the smallest emission as expected, which together with two-photon excitation spectroscopy yielded a single-particle bandgap of 6.08 eV at 10 K and a binding energy of free-exciton (FX) of  $E_x = 130 \text{ meV}$  in *h*-BN.<sup>[27]</sup>

A direct experimental measurement of the band-edge structure was performed on a lateral device fabricated from a *h*-BN quasi-bulk sample produced by HVPE via photocurrent excitation spectroscopy.<sup>[20]</sup> The room-temperature photocurrent excitation spectrum (PES) is shown in the inset of **Figure 2c**. The observed highest energy peaks correspond to the direct band-to-band photoexcitation at *M* point and *K* point, respectively, resolving the room-temperature minimum direct bandgap at *M*-point of  $E_g^M = 6.36 \text{ eV}$  and next lowest direct energy bandgap at *K*-point of  $E_g^K = 6.56 \text{ eV}$ . The two lowest energy peaks in the PES at 5.93 and 6.10 eV have been assigned to the optical excitation between *K* point of VBM to *M* point of the CBM assisted by either emitting or absorbing an LA phonon around *T* point with a wave vector  $\mathbf{q} = \mathbf{KM}$  to conserve the momentum and energy,<sup>[37]</sup> from which the room-temperature indirect bandgap of  $E_g^{\text{MK}} \approx 6.02 \text{ eV}$  and

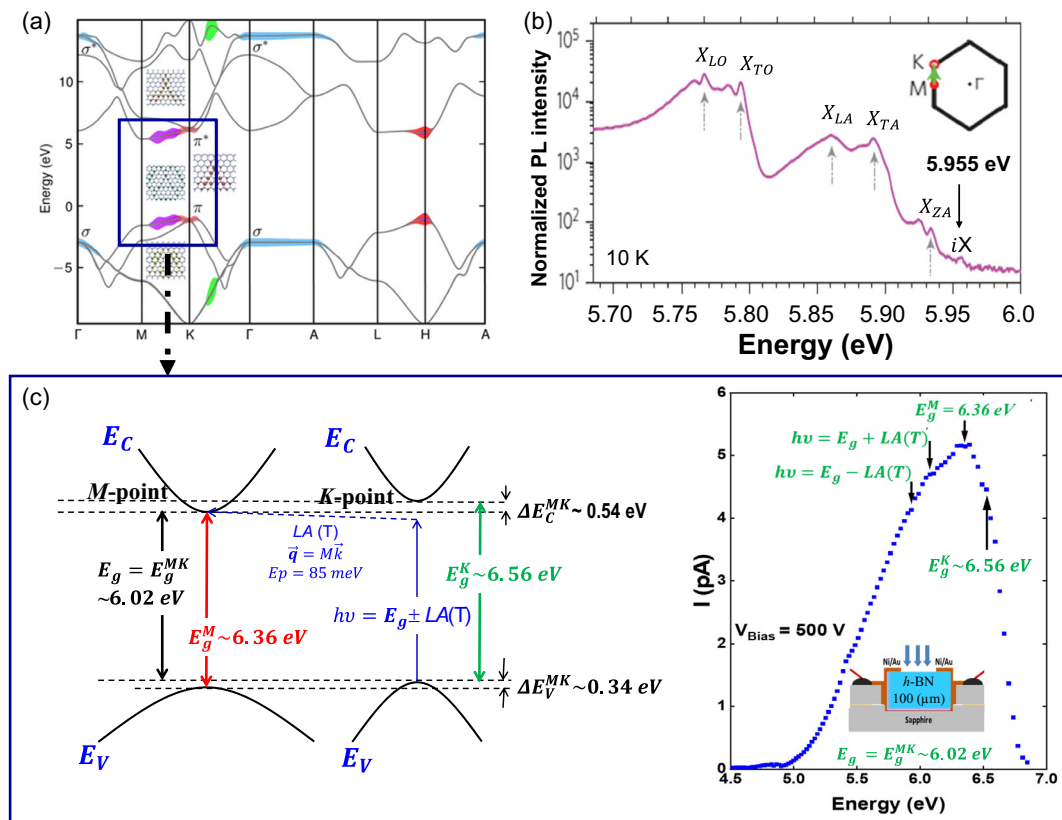


**Figure 2.** a) Calculated electronic band structure of bulk  $h$ -BN. The shaded regions represent the electron–hole density of states that contribute to the excitonic excitations projected along the  $h$ -BN band structure. Reproduced under terms of the CC-BY license.<sup>[38]</sup> Copyright 2024, The Authors. b) Phonon-assisted emission in  $h$ -BN, where  $iX$  denotes the “dark” exciton line. Reproduced with permission.<sup>[27]</sup> Copyright 2016, The Authors. c) Room-temperature energy band diagram near high symmetry  $K$  and  $M$  points in the first BZ of  $h$ -BN, constructed from the photocurrent excitation spectrum shown in the inset. Reproduced under terms of the CC-BY license.<sup>[20]</sup> Copyright 2024, The Authors.

energy differences between  $K$  and  $M$  points in the CBM and VBM —  $\Delta E_C^{MK} = 0.54$  eV and  $\Delta E_V^{MK} = 0.34$  eV, respectively—have been deduced. An energy band diagram near high symmetrical  $K$  and  $M$  points in the first BZ of  $h$ -BN constructed from the measured PES is shown in Figure 2c, whereas the energy differences between the CBM and VBM at  $M$  and  $K$  points estimated from Figure 2a are 0.54 eV ( $\Delta E_C^{MK}$ ) and 0.34 eV ( $\Delta E_V^{MK}$ ), respectively. Significantly differs from its III-nitride wurtzite counterparts, in which only electrons and holes in the conduction and valence band extremes at the  $\Gamma$  point are predominantly involved in the optical and transport processes, the results shown in Figure 2 highlight that charge carriers associated with both  $M$  and  $K$  valleys control the optical excitation, recombination, and charge transport processes in  $h$ -BN.

Despite its indirect bandgap nature, the unique features of  $h$ -BN in comparison with AlN are of immense interest for novel photonic device exploration, which can be briefly summarized later.<sup>[42–45]</sup>

### 2.1.1. High Optical Emission and Absorption

As shown in Figure 3a, PL emission intensity of the band-edge transitions in  $h$ -BN is typically more than 2 orders of magnitude higher than that of AlN at both 10 and 300 K from surface emission.<sup>[43,44]</sup> As shown in Figure 3b, early pioneering work has

provided a room-temperature energy bandgap of about 6 eV and an optical absorption coefficient of  $h$ -BN as high as  $7.5 \times 10^5 \text{ cm}^{-1}$  for the above bandgap photons.<sup>[23]</sup> If we adopt the concept of optical absorption of graphene for the above bandgap optical absorption in  $h$ -BN,<sup>[45]</sup> which states that its absorption is  $\pi e^2 / \hbar c = \pi \alpha = 2.3\%$ ,<sup>[46]</sup> with  $\alpha = e^2 / \hbar c = 1/137$  being the fine structure constant, we then have the optical absorption of  $h$ -BN = 2.3% per layer (3.33 Å). This gives the optical absorption length of about 14.5 nm and absorption coefficient for the above bandgap photons of  $7 \times 10^5 \text{ cm}^{-1}$ ,<sup>[45]</sup> agreeing exceptionally well with the measured value of  $7.5 \times 10^5 \text{ cm}^{-1}$ .<sup>[23]</sup> This implies that only a very thin layer of  $h$ -BN of  $\approx 70$  nm ( $\approx 5\lambda$ ) in thickness will absorb all the incoming above bandgap photons. It was shown that  $h$ -BN has an unusually strong  $p \rightarrow p$ -like transition due to the short bond length of B–N (1.55 Å). Moreover, the 2D nature of  $h$ -BN induces a sharp “step”-like density of states,  $g(\hbar\omega)$ , around the absorption edge.<sup>[44]</sup> These together give rise to exceptionally strong optical transitions near the absorption edge.

### 2.1.2. FX Binding Energy and Polarization of Band-Edge Emission in $h$ -BN

The reported FX binding energies,  $E_x$ , is more than 100 meV in  $h$ -BN bulk crystals.<sup>[25,27,35,36]</sup>  $E_x$  is expected to increase with

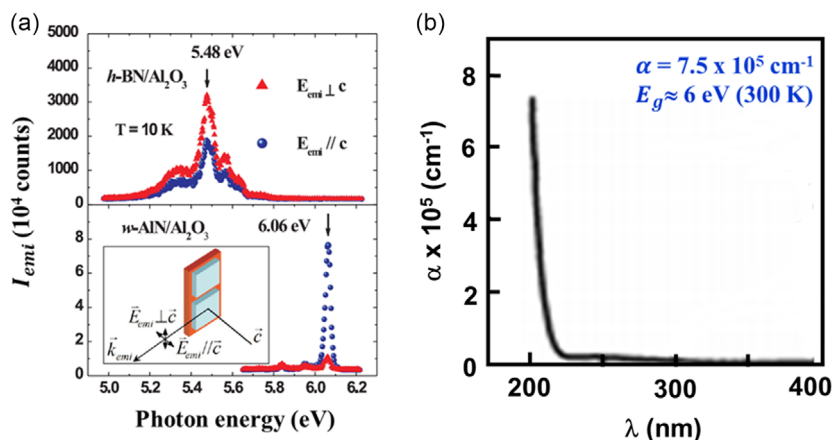


**Figure 3.** a) Comparison of band-edge PL spectra of *h*-BN and AlN epilayers measured at a) 10 K and b) 300 K. Reproduced with permission.<sup>[44]</sup> Copyright 2012, American Physical Society. b) Optical absorption coefficient versus wavelength. Reproduced with permission from inset of Figure 4.<sup>[23]</sup> Copyright 1997, The Japan Society of Applied Physics (JSAP).

decreasing the *h*-BN layer thickness. Due to its unique crystalline and electronic structures, the material system is known to exhibit an unusually strong phonon and charge carrier interaction.<sup>[27,37,38,40,41]</sup> Polarization-resolved PL measurements shown in Figure 3a and theoretical calculations have determined that the band-edge emission in *h*-BN is predominantly transverse-electric polarized<sup>[43,44]</sup> in contrast to the well-known transverse-magnetic polarization in AlN, first demonstrated by the present authors 20 years ago.<sup>[39,47]</sup>

## 2.2. Other Basic Parameters

One of the most important parameters of an electronic material is its breakdown field ( $E_B$ ). The breakdown field of *h*-BN in the direction of parallel to the *c* axis has been measured by several groups for a few layers and multiple layers exfoliated from high-quality *h*-BN bulk crystals synthesized by HPHT method<sup>[28,29,48]</sup> as well as for epitaxial films synthesized by metal-organic

chemical vapor deposition (MOCVD).<sup>[45]</sup> The values of  $E_B$  in the directions of normal and parallel to the *c* axis ( $E_{B\perp c}$  and  $E_{B\parallel c}$ ) have been measured under a well-controlled relative humidity.<sup>[28,29]</sup> As shown in Figure 4a,b, the breakdown field along the *c* axis,  $E_{B\parallel c}$ , increases continuously with decreasing the layer thickness<sup>[28]</sup> and approaches 20 MV cm<sup>-1</sup> for a few layers of *h*-BN<sup>[48]</sup> with a bulk value of  $E_{B\parallel c}$  ( $\approx 12$  MV cm<sup>-1</sup>), exceeding that of diamond.<sup>[29]</sup> The values measured in thin films produced by MOCVD is consistently lower, which clearly implies that  $E_{B\parallel c}$  strongly depends on the crystalline quality. Due to its layered crystalline structure, most physical properties of *h*-BN are also anisotropic. Compared to  $E_{B\parallel c}$ , the measured in-plane breakdown field,  $E_{B\perp c}$ , is about 3 MV cm<sup>-1</sup>.<sup>[28,29]</sup>

The thermal conductivity and the anisotropy of thermal conductivity of high-quality single-crystal *h*-BN grown by a metal flux solution method have been measured for natural and <sup>10</sup>B and <sup>11</sup>B isotope-enriched *h*-BN.<sup>[30]</sup> The results shown in Figure 5 revealed that natural *h*-BN, containing 20% <sup>10</sup>B and 80% <sup>11</sup>B,

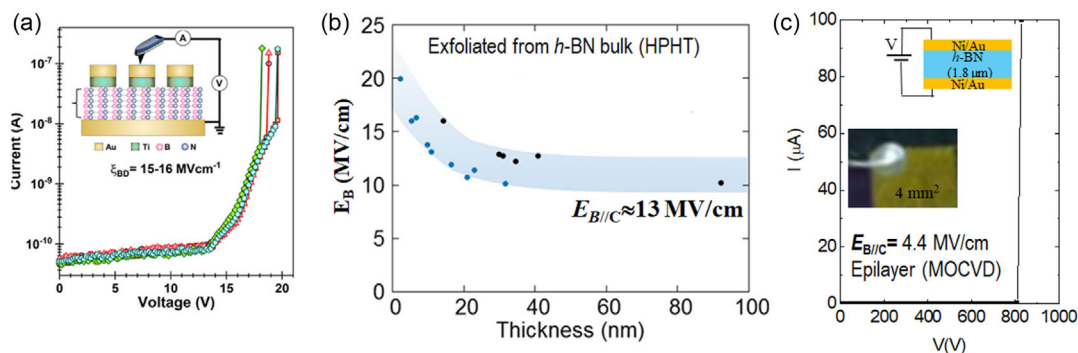


**Figure 4.** a,b) Breakdown fields in the direction parallel to the *c* axis,  $E_{B\parallel c}$ , measured in *h*-BN exfoliated from high-quality *h*-BN bulk single crystals using conduction atomic force microscopy (AFM) technique. (a) Measurement of  $E_{B\parallel c}$  for various devices consisting of *h*-BN with 7–19 nm in thickness. Reproduced under terms of the CC-BY license.<sup>[48]</sup> Copyright 2021, The Authors. (b)  $E_{B\parallel c}$  as a function of *h*-BN layer thickness. Reproduced with permission.<sup>[23]</sup> Copyright 2015, American Chemical Society. (c)  $I$ – $V$  characteristics of a *h*-BN epilayer of 1.8  $\mu\text{m}$  in thickness released from sapphire substrate measured in the *c* direction. Insets show a schematic of an *h*-BN epilayer released from the sapphire substrate for breakdown field measurement and the structure having a cross-sectional area of about  $\approx 4$  mm<sup>2</sup>. Reproduced with permission.<sup>[45]</sup> Copyright 2012, AIP Publishing LLC.

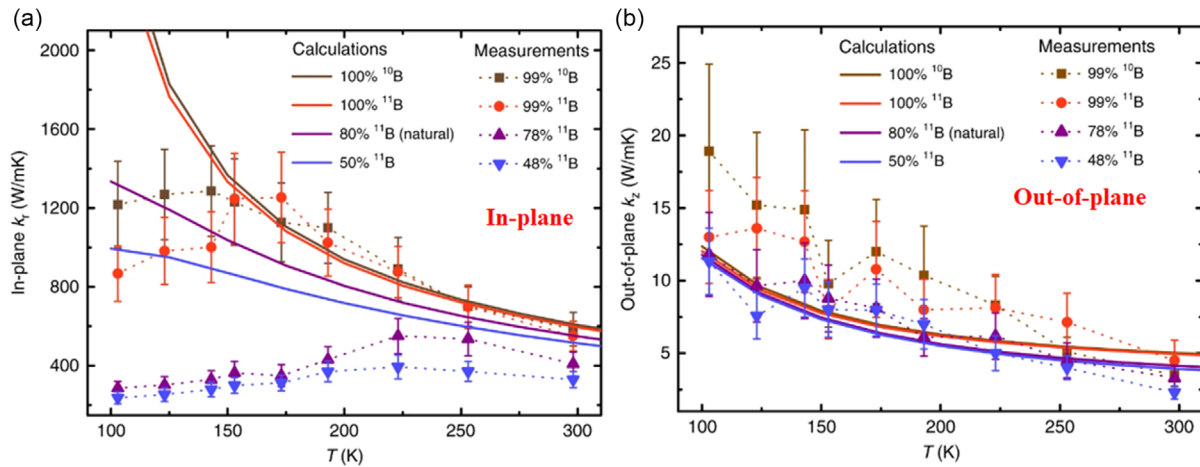


**Figure 5.** Temperature-dependent thermal conductivities and anisotropic ratio of *h*-BN crystals, and comparison with model predictions: a) in-plane thermal conductivity; b) out-of-plane thermal conductivity. Reproduced under terms of the CC-BY license.<sup>[30]</sup> Copyright 2019, The Authors.

exhibits an in-plane thermal conductivity,  $\kappa_{\perp c}$ , of about  $550 \text{ W m}^{-1} \text{ K}^{-1}$ , whereas the out-of-plane thermal conductivity,  $\kappa_{\parallel c}$ , is about 2 orders of magnitude lower.<sup>[30]</sup>

The anisotropic index of refraction of *h*-BN has also been measured using a  $200 \mu\text{m}$  thick  $^{10}\text{B}$  isotope enriched *h*-BN (*h*- $^{10}\text{BN}$ ) freestanding quasi-bulk sample using spectroscopic ellipsometry in the UV (4.0–5.1 eV) spectral range.<sup>[49]</sup> This thick sample was shown to contain turbostratic (*t*-) phase domains based on X-ray diffraction (XRD) characterization. It was found that the index of refraction for the polarization mode with electric field perpendicular to the *c* axis (ordinary,  $n_o$ ) is much higher than that with electric field parallel to the *c* axis (extraordinary,  $n_e$ ). By taking into account of turbostratic- (*t*-) phase layers within *h*-BN having an average inclination angle ( $\theta$ ) with respect to the ideal *c* plane, as schematically illustrated in **Figure 6a**, a simple method for quantifying  $\theta$  has been deduced. The results revealed that

the presence of *t*-phase domains decreases the optical anisotropy of *h*-BN and that a signature of improved crystalline quality is an increase in the ordinary index of refraction ( $n_o$ ) as the average incline angle  $\theta$  approaching to  $0^\circ$ . As shown in **Figure 6b**, The spectroscopic ellipsometry measurement predicted that  $n_o = 2.7$  and  $n_e = 1.5$  at 280 nm for a perfect *h*-BN crystal. In comparison, the measured static in-plane and out-of-plane dielectric constants are 6.85 and 5.06, respectively.<sup>[50]</sup>

Another unique property of *h*-BN is that isotope  $^{10}\text{B}$  has a large capture cross section ( $\sigma$ ) of about 3840 barns ( $=3.84 \times 10^{-21} \text{ cm}^2$ ) for thermal neutrons (neutrons with an average energy = 25 meV), which is only slightly smaller than a value of  $\sigma \approx 5330$  barns for He-3.<sup>[31,32]</sup> However, as a semiconductor material, the density of atoms which can interact with thermal neutrons in 100%  $^{10}\text{B}$ -enriched *h*-BN (*h*- $^{10}\text{BN}$ ) is  $N(^{10}\text{B}) = 5.5 \times 10^{22} \text{ cm}^{-3}$ , which is about 550 times higher than that in a He-3 gas tube

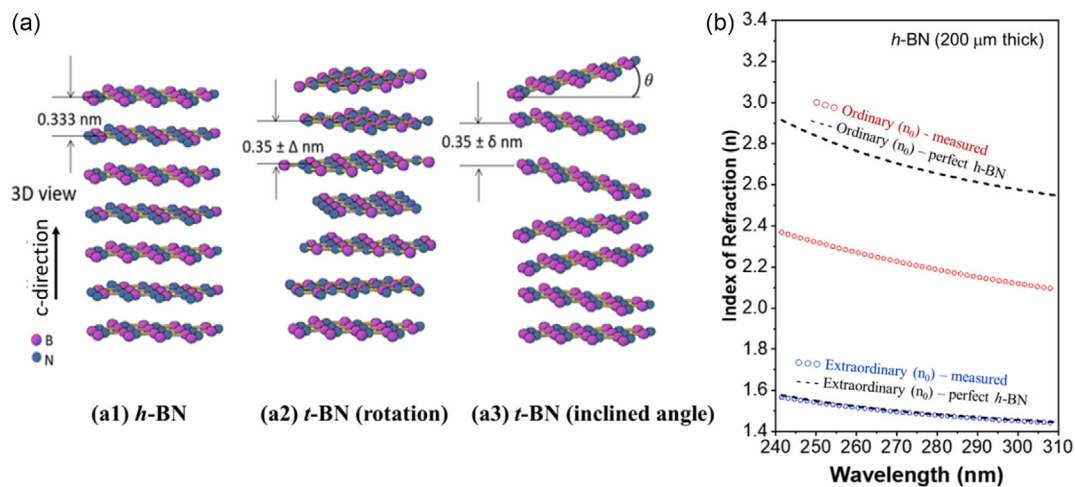


**Figure 6.** a) Schematic diagram of the microstructure of *t*-phase *h*-BN layer orientation relative to the ideal *c* plane. b) Indices of refraction ( $n$ ) of a  $200 \mu\text{m}$  thick *h*- $^{10}\text{BN}$  quasi-bulk wafer in the UV range measured using spectroscopic ellipsometry for both polarization modes with electric field perpendicular ( $n_o$ ) and parallel ( $n_e$ ) to the *c* axis as functions of incident wavelength  $\lambda$  (open circles) and expected index of refraction of a perfect single-crystal *h*-BN (dotted curves). Reproduced with permission.<sup>[49]</sup> Copyright 2012, AIP Publishing LLC.

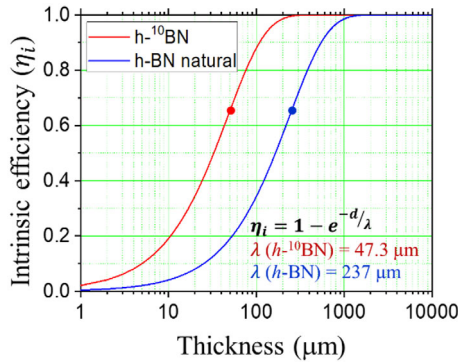


**Figure 7.** Plot of thermal neutron absorption or the theoretical thermal neutrons detection efficiency of  $h\text{-}^{10}\text{BN}$  (red curve) and  $h\text{-BN}$  (blue curve) versus the detector's thickness.

pressurized at 4 atm. This provides a thermal neutron absorption coefficient of  $\alpha = N\sigma = 5.5 \times 10^{22} \times 3.84 \times 10^{-21} = 211.2 \text{ cm}^{-1}$  and an absorption length of  $\lambda = \alpha^{-1} = 47.3 \mu\text{m}$  in  $h\text{-}^{10}\text{BN}$ .<sup>[51–58]</sup>

The thermal neutron absorption or equivalent the theoretical detection efficiency ( $\eta_i$ ) of  $h\text{-}^{10}\text{BN}$  detectors as a function the detector's layer thickness,  $d$ , can be expressed as

$$\eta_i = 1 - e^{-d/\lambda} \quad (1)$$

where  $\lambda(h\text{-}^{10}\text{BN}) = 47.3 \mu\text{m}$  (thermal neutron absorption length). Element B exists as two main isotopes,  $^{10}\text{B}$  and  $^{11}\text{B}$  in a natural abundance of  $\approx 20$  and  $80\%$  respectively,<sup>[31,32]</sup> meaning that the thermal neutron absorption length in natural  $h\text{-BN}$  is  $\lambda(h\text{-BN}) = 237 \mu\text{m}$ .<sup>[51–58]</sup> **Figure 7** plots the theoretical detection efficiency ( $\eta_i$ ) as a function of detector's thickness for both  $h\text{-}^{10}\text{BN}$  and  $h\text{-BN}$ . The results imply that  $h\text{-}^{10}\text{BN}$  ( $h\text{-BN}$ ) with a thickness of  $\approx 5\lambda = 47.3 \mu\text{m}$  ( $237 \mu\text{m}$ ) in thickness will capture nearly all the incoming thermal neutrons. **Figure 7** clearly shows the need for thick  $h\text{-BN}$  quasi-bulk wafers to obtain high-efficiency thermal neutron detectors. In comparison,

in He-3 gas detectors, enhancement in the detection sensitivity is achieved through increasing the gas tube diameter, length, and gas pressure.

### 3. HVPE Growth and Properties of $h\text{-BN}$ Quasi-Bulk Crystals

Bulk crystals of  $h\text{-BN}$  produced by HPHT techniques<sup>[24,26–29,59–61]</sup> and metal flux solution methods<sup>[30,38,62]</sup> possess very high-crystalline and optical qualities but are impractical to serve as substrates or for device implementation, as their sizes are typically millimeters. The development of crystal growth technologies for producing thick epitaxial films (or quasi-bulk crystals) in large wafer sizes with high-crystalline quality is a prerequisite for utilizing  $h\text{-BN}$  as an UWBG electronic and photonic material. Moreover, as shown in **Figure 7**, thermal neutron detectors also require the development of quasi-bulk crystals with large thicknesses to provide high detection efficiency. Here, we provide a brief overview of recent developments in producing  $h\text{-BN}$  quasi-bulk crystals and high-efficiency  $h\text{-BN}$  neutron detectors achieved exclusively by our group.

#### 3.1. HVPE Growth and Structural Properties

**Table 1** compares general features of three most established thin film growth techniques, HVPE, MOCVD, and molecular beam epitaxy (MBE). Earlier pioneering works on MOCVD growth of  $h\text{-BN}$  epilayers have been thoroughly reviewed in one of our previous publications.<sup>[42]</sup> Thermal neutron detection has been successfully demonstrated using MOCVD grown  $h\text{-}^{10}\text{BN}$  epilayers.<sup>[51–58]</sup> The growth of  $h\text{-BN}$  thin epilayers by MBE has also been demonstrated by several groups.<sup>[63–65]</sup> More recently, thin  $h\text{-BN}$  epilayers grown on sapphire substrates with a diameter up to 6 inches have been achieved using MOCVD.<sup>[66]</sup> While the growth rate of MOCVD is typically limited to a few micrometers per hour, posing significant challenges in producing

**Table 1.** Comparison of general features of three major semiconductor epitaxial growth methods.

Features	HVPE	MOCVD	MBE
Growth mechanism	Vapor-phase deposition using hydrides which are carbon free	Chemical vapor deposition using metal-organic compounds, inherently containing carbon impurities	Physical deposition using molecular beams
Material types	Primarily used for III–V and II–VI semiconductors	Suitable for a wide range of materials including III–V and II–VI semiconductors	Primarily used for III–V and II–VI semiconductors
Growth temperature	High (typically 700–1500 °C)	Moderate to high (typically 600–1400 °C)	Low to moderate (typically 200–1000 °C)
Growth rate	Very high (up to 100 $\mu\text{m h}^{-1}$ )	Moderate (1–5 $\mu\text{m h}^{-1}$ )	Low (up to $\approx 1 \text{ \AA s}^{-1}$ or $\approx 360 \text{ nm h}^{-1}$ )
Uniformity	Good uniformity	Good uniformity	Excellent uniformity
Control over composition	Moderate control	Good control over composition and doping	Excellent control over composition and doping
System complexity	Less complex than MOCVD and MBE	Moderate complexity; may require handling of toxic gases	High complexity; requires ultrahigh vacuum conditions
Cost	Generally lower operational costs	Moderate to high operational costs	High initial and operational costs
Applications	Substrates and epilayers for advanced semiconductor devices	Epilayers, quantum wells, superlattices, and advanced semiconductor devices	Epilayers, quantum wells, superlattices, and advanced semiconductor devices

*h*-BN quasi-bulk wafers, the extremely low growth rate of MBE makes the growth of *h*-BN quasi-bulk wafers an impossible task. Among these techniques, HVPE is a proven epitaxial growth technique capable of producing high-quality GaN<sup>[67]</sup> and AlN<sup>[33,34]</sup> at much higher growth rates than MOCVD and MBE. Moreover, the precursors for HVPE growth are carbon free.<sup>[33,34,67–69]</sup> HVPE growth of high-quality AlN quasi-bulk crystals at a high growth rate relies on the abilities of achieving a sufficiently high growth temperature and suppression of parasitic reactions.<sup>[33,34]</sup> Figure 8a shows an early study of AlN growth by HVPE, which revealed that crystalline quality enhances with increasing the growth temperature, as assessed by the full-width at half-maximum (FWHM) of XRD rocking curves of the (0002) and (10  $\bar{1}0$ ) planes of AlN.<sup>[33]</sup>

More recently, the optimal HVPE growth temperature for AlN has been established to be around 1450 °C.<sup>[34]</sup> To suppress the parasitic reactions, the improved HVPE system, which is designed by Nippon (TAIYO NIPPON SAN SO (HVPE-A111)) for AlN growth, is a quartz-based horizontal atmospheric-pressure HVPE reactor comprising an upstream region (source zone) heated by an electric furnace and a downstream region (growth zone) heated by RF induction. AlCl<sub>3</sub> gas, the Al source, was generated by supplying HCl gas using H<sub>2</sub> as a carrier gas to the source zone filled with Al metal pellets, maintained at 500 °C. To avoid parasitic reaction between the N source (NH<sub>3</sub>) and Al source (AlCl<sub>3</sub>), the AlCl<sub>3</sub> was supplied to the growth zone through a double nozzle made of BN from the center and N<sub>2</sub> gas flows from the periphery as a separation gas. The flow direction of AlCl<sub>3</sub> was parallel to the surface of the susceptor, whereas NH<sub>3</sub> was supplied from diagonally above the susceptor using H<sub>2</sub> carrier gas through a BN nozzle, separate from the AlCl<sub>3</sub>. Figure 8b shows the input partial pressure of HCl ( $P_{\text{HCl}}^0$ ) dependence of the growth rate for AlN homoepitaxial layers. At a growth temperature of 1450 °C, the growth rate was observed to increase linearly with increasing  $P_{\text{HCl}}^0$ , and a high growth rate of over 150  $\mu\text{m h}^{-1}$  was achieved. Additionally, at this growth rate, the resulting AlN retains the

structural quality of the native AlN substrate grown by physical vapor transport, as demonstrated through the measured FWHMs of XRD rocking curves of the (0002) and (10  $\bar{1}0$ ) planes of AlN of 15 and 19 arcsec, respectively, independent of the growth rate.<sup>[34]</sup>

Overall, the HVPE growth processes for producing high-quality *h*-BN must deal with similar challenges as for AlN, which also require the abilities to support high growth temperatures typically above 1400 °C and mitigate the issue of parasitic reactions in the gas phase. To grow *h*-BN wafers, BCl<sub>3</sub> and NH<sub>3</sub> gases were used as precursors.<sup>[20,70–72]</sup> The growth was conducted on *c*-plane sapphire. At a growth temperature of 1450 °C, the growth rate was about 15  $\mu\text{m h}^{-1}$ . As illustrated in Figure 9a, due to its layered crystalline structure, *h*-BN self-separates from sapphire to form a freestanding and flexible wafer during cooling process after growth<sup>[20,49,54–58,70–72]</sup> and as such, the concept of wafer bowing is likely not applicable to *h*-BN quasi-bulk wafers. Moreover, these wafers do not self-delaminate during the growth process. This self-separation phenomenon offers several benefits, allowing wafer dicing more easily, reuse of sapphire substrates, and the fabrication of devices in flexible forms (e.g., stacked or curved configurations).

Figure 9b shows XRD pattern in  $2\theta - \omega$  scan of a 100  $\mu\text{m}$  thick freestanding *h*-BN quasi-bulk wafer synthesized by HVPE, revealing the *h*-BN (002) peak position (diffraction from stacked planes in the *c* direction) centered at  $2\theta = 26.72^\circ$ , corresponding to a *c*-lattice constant of nearly 6.66 Å, corroborating the TEM measurements results shown in Figure 1b. Shown in Figure 9c is the XRD in  $2\theta - \omega$  scan in a large angle range. Diffraction peaks from *h*-BN (002), (004), and (006) planes (stacked planes in the *c* direction) are clearly observable, which indicates that these *h*-BN quasi-bulk crystals have a very good long-range order along the *c* axis. Figure 9d plots a Raman spectrum of a freestanding *h*-BN quasi-bulk wafer.<sup>[20]</sup> The observed mode at  $\Delta\sigma = 1366 \text{ cm}^{-1}$  is related to the  $E_{2g}$  vibration mode (in-plane stretch of B and N atoms) and corresponds well with the expected Raman peak of bulk *h*-BN,<sup>[61]</sup> suggesting that these freestanding HVPE wafers are strain free.

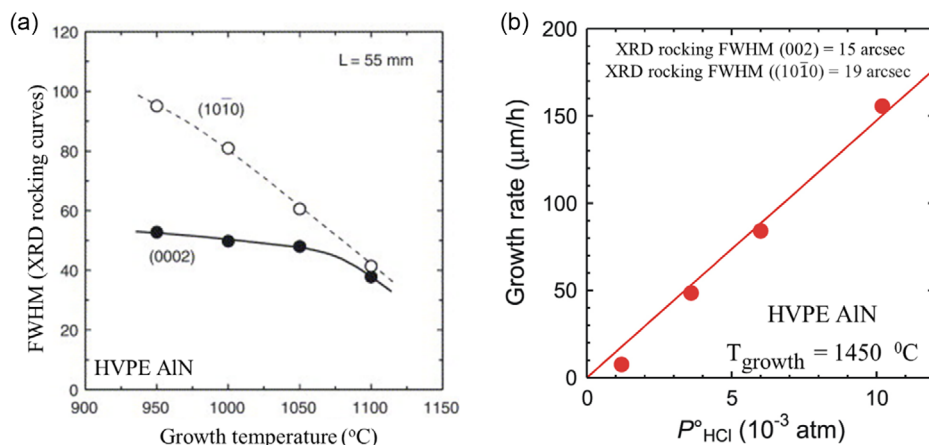


**Figure 8.** a) FWHMs of XRD rocking curves of the (0002) and (10  $\bar{1}0$ ) planes of AlN epilayers grown at various temperatures for 1 h, where  $L$  is the distance between the end of the injection nozzle and sapphire substrate. Reproduced with permission.<sup>[33]</sup> Copyright 2005, Elsevier B.V. b) Partial pressure of HCl dependence of the growth rate of AlN homoepitaxial layers on AlN (0001) substrates at 1450 °C by HVPE. Reproduced with permission.<sup>[34]</sup> Copyright 2022, The Japan Society of Applied Physics (JSAP).

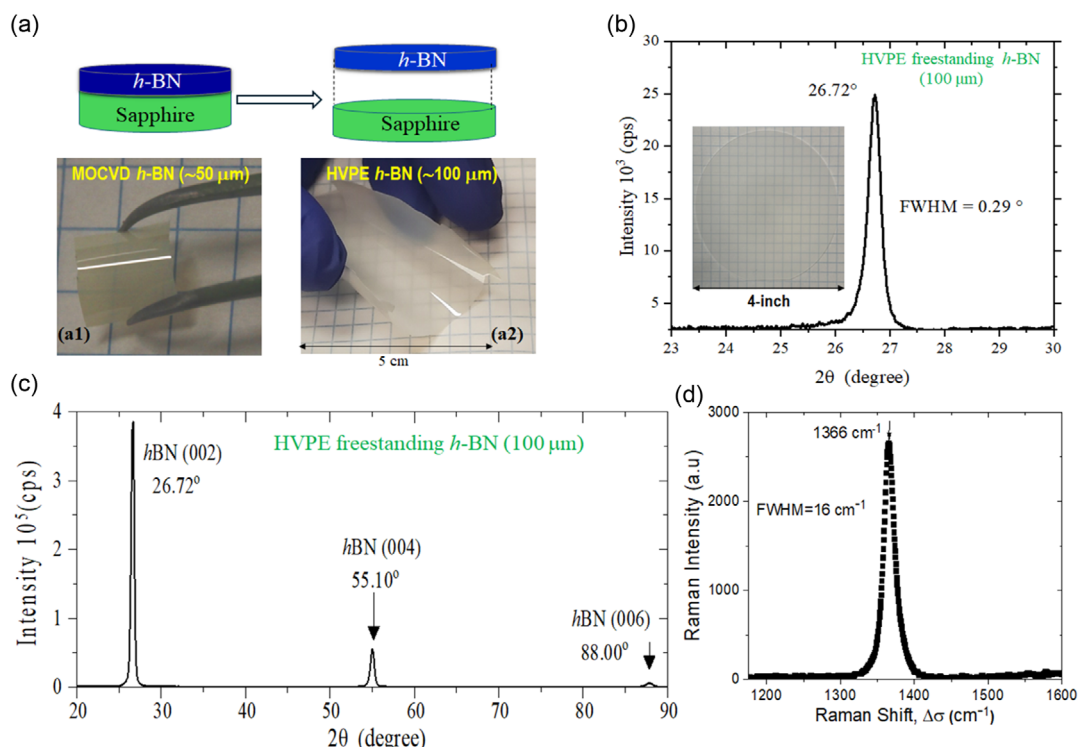


**Figure 9.** Freestanding *h*-BN quasi-bulk wafers: a) Schematic illustration for realizing freestanding *h*-BN wafer by self-separation during cooling down after growth. a1,a2) Photos of flexible *h*-BN freestanding wafer produced by MOCVD and HVPE, respectively. Reproduced with permission.<sup>[55]</sup> Copyright 2017, AIP Publishing LLC. b,c) XRD pattern in  $2\theta$ - $\omega$  scans from b) 23–30° and c) 20–90° of a 100  $\mu\text{m}$  thick freestanding and flexible *h*-BN quasi-bulk wafer synthesized by HVPE. (a2–c) Reproduced under terms of the CC-BY license.<sup>[72]</sup> Copyright 2024, The Authors. d) Room-temperature Raman spectrum of a 100  $\mu\text{m}$  thick *h*-BN quasi-bulk wafer produced by HVPE. Reproduced under terms of the CC-BY license.<sup>[20]</sup> Copyright 2024, The Authors.

The TEM result shown in Figure 1b, and XRD and Raman results shown in Figure 9 all indicate that HVPE quasi-bulk crystals have a pure *h* phase (layered structure). Since the  $E_{2g}$  vibration mode results from the in-plane stretch of B and N atoms, its FWHM directly correlates with the structural ordering in the *c* plane. The observed FWHM of the  $E_{2g}$  vibration mode in HVPE quasi-bulk wafers of  $16\text{ cm}^{-1}$  is much broader than those seen in *h*-BN bulk crystals grown by high temperature and high pressure (HTHP) of typically  $8\text{--}10\text{ cm}^{-1}$ .<sup>[61]</sup> Moreover, the FWHM of the Raman peak in *h*-<sup>10</sup>BN quasi-bulk wafers is comparable to that of natural *h*-BN. This contrasts sharply with high-quality *h*-BN bulk crystals grown via metal flux solution. In these crystals, isotopic enrichment (*h*-<sup>10</sup>BN and *h*-<sup>11</sup>BN) leads to a substantial reduction in the FWHM to  $1\text{--}2\text{ cm}^{-1}$  compared to  $8\text{--}10\text{ cm}^{-1}$  observed in natural *h*-BN.<sup>[73]</sup> This comparison suggests that the FWHM of the Raman peak in the HVPE-grown quasi-bulk *h*-BN is far from intrinsic values, indicating that the crystalline quality of our HVPE-grown material is considerably lower than that obtained through metal flux solution or HPHT methods.

The thickest and largest diameter HVPE *h*-BN quasi-bulk wafers produced by our group as of this writing are  $\approx 1\text{ mm}$  and  $6''$ , respectively. While the challenge of wafer scalability in thickness primarily arises from a very long growth time even with a growth rate of  $15\text{ }\mu\text{m h}^{-1}$ , the scalability in wafer size primarily arises from limited surface migration of boron atoms,

which is due to the strong B–N bond, as well as the significant parasitic reactions that occur between boron and nitrogen precursors in the gas phase. Our recent successful synthesis of thick  $6''$ -diameter *h*-BN quasi-bulk wafers was made possible by utilizing inert nitrogen ( $\text{N}_2$ ) as both the carrier and purging gas, along with implementing low-pressure growth conditions to minimize these parasitic reactions. Further detailed results regarding this accomplishment will be reported in a separate publication. However, the overall crystalline quality deteriorates with increasing the wafer thickness. This is in contrast to the AlN, in which defects and dislocations tend to self-annihilate with increasing AlN layer thickness.<sup>[74]</sup> For instance, for  $400\text{ }\mu\text{m}$  thick *h*-BN wafers, XRD patterns in  $2\theta$ - $\omega$  scans indicated that the *h*-BN (002) peak appears at an angle of  $2\theta = 26.56^\circ$  corresponding to an interlayer spacing that is slightly larger than  $3.33\text{ \AA}$ ,<sup>[75]</sup> compared to  $2\theta = 26.72^\circ$  for  $100\text{ }\mu\text{m}$  thick *h*-BN wafers shown in Figure 9. Moreover, we have also carried out XRD analysis focused on the bottom surface (the surface attached to the sapphire substrate during growth) and the top surface. The XRD results indicated that the XRD intensity measured from the bottom surface is consistently higher than that measured from the top surface. These results lead to the conclusion that crystalline quality degrades as the layer thickness increases.

Furthermore, the nature and density of dislocations or defects in *h*-BN, particularly given its layered structure, remain less understood compared to GaN and AlN. Applying established

methods for defect density estimation used in GaN and AlN, the defect density is estimated through the analysis of the XRD rocking curve linewidth. This analysis suggests a structural defect density exceeding  $10^{10} \text{ cm}^{-2}$ , as we discussed for *h*-BN epilayers.<sup>[76]</sup> The layered crystalline structure of *h*-BN introduces unique defect types, including layer sliding, tilt, rotation, and *t*-phase domains, as illustrated in Figure 6a. The prevalence of these structural disorders appears to increase with layer thickness during growth. Therefore, continued efforts to enhance structural order, both along the *c* axis and within the *c* plane, are crucial. Specifically, the development of HVPE growth systems with improved temperature capabilities is highly desirable.

### 3.2. PL and Anisotropy of Transport Properties

It has been universally observed that the low-temperature band-edge PL spectra of high-quality *h*-BN bulk materials consist of two groups of optical transitions, multiple sharp peaks designated as the S (sharp) lines in the spectral range of 5.75–5.95 eV and more diffused bands labeled as D lines in the spectral range of 5.4–5.7 eV.<sup>[24,27,41,75–80]</sup> Because *h*-BN has an indirect energy bandgap, it is understood now that the observed S and D lines in *h*-BN bulk crystals can be attributed to phonon-assisted FX transitions involving various phonon modes at *T* point in the first BZ to satisfy the requirement of momentum conservation.<sup>[27]</sup> The observation of FX-related recombination lines is considered a hall mark of high-quality materials. In comparison, the room-temperature PL emission spectrum of *h*-BN quasi-bulk sample produced by HVPE presented in Figure 10 exhibits a dominant emission line near 3.6 eV and a weak band-edge emission peak near 5.9 eV.<sup>[81]</sup> The origin of the 3.6 eV emission line was thought to be related to native defects.<sup>[71,72]</sup> The observation of the weak band-edge emission near 5.9 eV suggests that these quasi-bulk crystals have a decent crystalline quality, in agreement with the XRD results shown in Figure 8. However, the results

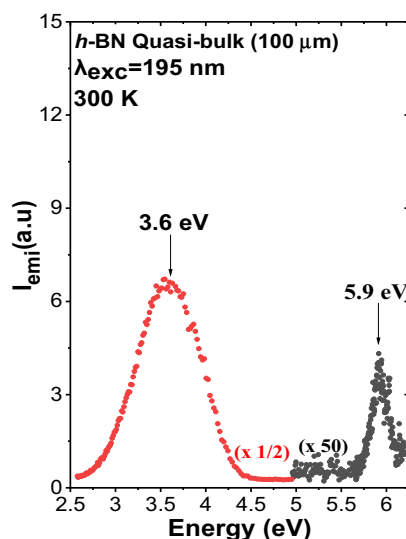


**Figure 10.** A Room-temperature PL emission spectrum of a 100  $\mu\text{m}$  thick freestanding *h*-BN quasi-bulk wafer synthesized by HVPE. Reproduced with permission.<sup>[77]</sup> Copyright 2024, AIP Publishing LLC.

of impurity recombination line being dominant in *h*-BN quasi-bulk crystals shown in Figure 10 indicate that the overall material quality is still some distance away from those of the state-of-the-art *h*-BN bulk crystals<sup>[24,27,76,78–80]</sup> and thin epitaxial layers produced by MOCVD.<sup>[41–45]</sup> By monitoring the intensity ratio of the band edge to native defect-related emission lines, in tandem with XRD, PL measurements have proven to be an effective technique to guide the growth optimization processes to suppress native defects in Al-rich AlGaIn.<sup>[82,83]</sup> Currently, we are adopting the same approach to further advance the *h*-BN growth processes by HVPE.

Many physical properties of *h*-BN are anisotropic due to its layered structure, such as thermal conductivity and refractive index, as demonstrated in Figure 5 and 6. An anisotropic behavior is also expected for the carrier transport properties in *h*-BN, i.e., the lateral transport properties are superior to those in the vertical direction, which has a profound consequence on the device implementation. Due to its UWBG nature, *h*-BN exhibits exceptionally high dark electrical resistivities, typically exceeding  $1 \times 10^{13} \Omega\text{-cm}$  at room-temperature.<sup>[54–58,70–72]</sup> This high resistivity impedes Ohmic contact formation and renders traditional Hall-effect measurements challenging.

In contrast, photocurrents are relatively easy to measure because the dark currents are very low in *h*-BN devices. By measuring the applied electric field dependence of photocurrent, the charge carrier mobility-lifetime ( $\mu\tau$ ) products can be obtained from a classical description for large bandgap insulating materials.<sup>[84,85]</sup> The quantity of  $\mu\tau$  is strongly influenced by the overall material quality and is one of the most important transport parameters for determining the device's performance. For instance, it is well established that in *a*-Si: H *p*–*i*–*n* solar cells the cell efficiency is strongly correlated with the  $\mu\tau$  products of the *i*-layer.<sup>[86]</sup> Similarly, for CdTe and CdZnTe radiation detectors, a high  $\mu\tau$  product is crucial for achieving high detection efficiency. This parameter facilitates the effective collection of radiation-generated charge carriers at the electrodes, significantly reducing losses due to recombination and trapping.<sup>[87]</sup> Monitoring the  $\mu\tau$  products has been very effective in guiding the development of *h*-BN quasi-bulk crystal for neutron detectors. The  $\mu\tau$  products of our *h*-BN materials have been improved by several orders of magnitude from  $10^{-8}$ <sup>[52]</sup> to  $>10^{-4} \text{ cm}^2 \text{ V}^{-1}$ ,<sup>[54–57,70–72,88]</sup> leading to the realization of *h*-<sup>10</sup>B thermal neutron detectors with a record high detection efficiency of  $\approx 60\%$ .<sup>[57,72]</sup>

The anisotropic effects on the carrier transport properties of *h*-BN have been measured by measuring the  $\mu\tau$  products of both vertical and lateral devices, which made possible by using *h*-BN quasi-bulk crystals. The fabrication processes for vertical detectors include 1) dicing *h*-BN wafers into desired shapes and dimensions followed by 2) depositing top and bottom contacts consisting of a bilayer of Ni (100 nm)/Au (40 nm) using e-beam evaporation, as illustrated in Figure 11a. The fabrication processes of lateral devices include the following steps: 1) dicing freestanding *h*-BN wafer into detector strips; 2) mount detector strips on sapphire using a highly resistive adhesive material; and 3) a mask was fabricated and used to deposit metal contacts consisting of a bilayer of Ni (100 nm)/Au (40 nm) on the clipped edges of the *h*-BN strips using e-beam evaporation, leaving around  $\approx 100 \mu\text{m}$  of metal covering on the two edges.<sup>[56–58,70–72]</sup>

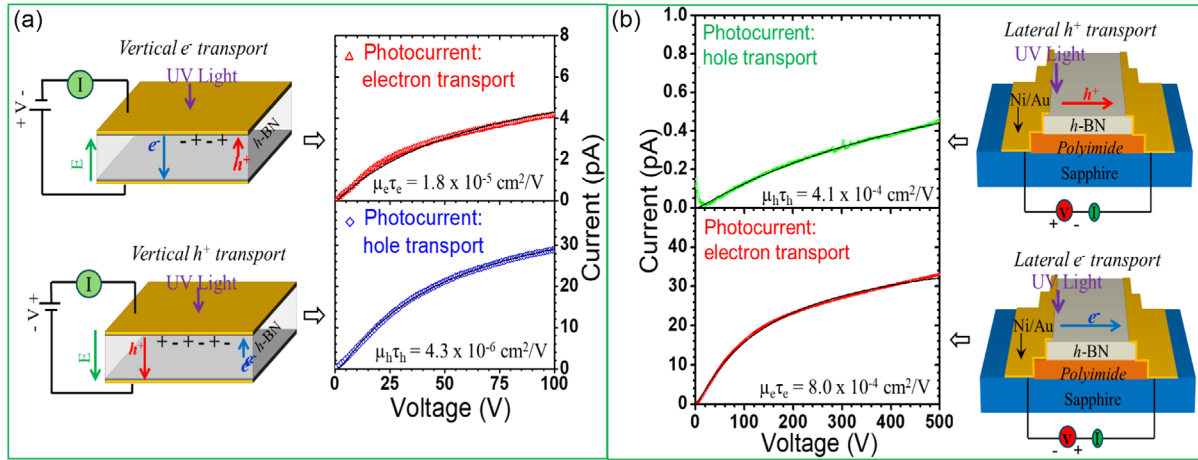


**Figure 11.** Photocurrent–voltage characteristics of *h*-BN quasi-bulk wafers measured in the a) vertical direction and b) lateral direction. Experimental geometry enables the characterization of the electron- and hole-transport properties separately. (a) Reproduced with permission.<sup>[88]</sup> Copyright 2018, AIP publishing LLC. (b) Reproduced with permission.<sup>[56]</sup> Copyright 2018, AIP publishing LLC.

The schematic illustration of these lateral detectors is depicted in Figure 11b.

In *h*-BN, due to its layered structure, the optical absorption coefficient is exceptionally large and is  $7.5 \times 10^5 \text{ cm}^{-1}$ , as shown in Figure 3b, which translates to an optical absorption length of the above-bandgap photons of only about 15 nm.<sup>[23,42,45]</sup> This property enables us to characterize vertical electrical transport properties for photogenerated electrons and holes separately, as schematically illustrated in Figure 11a. Depending upon the polarity of the illuminated surface, a specific charge carrier type (hole or electron) can be selected for charge transport in the vertical direction. In the experimental configuration shown at the top (bottom) of Figure 11a, holes (electrons) are rapidly extracted by the illuminated top cathode (anode). This allows for the transport property of electrons (holes) to be probed.<sup>[54,55,88]</sup> The photocurrent–voltage (*I*–*V*) characteristics under UV excitation can be utilized to extract  $\mu\tau$  using the classical Many’s equation for insulating semiconductors by taking into consideration both the effects of surface recombination and bulk trapping, by assuming that the contacts are perfectly blocking type for simplicity<sup>[84,85]</sup>

$$I(V) = I_0 \frac{V_{\mu\tau} \left( 1 - e^{-\frac{W^2}{V_{\mu\tau}}} \right)}{W^2 \left( 1 + \frac{S W}{\mu V} \right)} \quad (2)$$

where  $\mu\tau$  denotes the mobility-lifetime product of photogenerated charge carriers, *W* the carrier drift length (or *h*-BN layer thickness for vertical devices), *V* the bias voltage, and *S* the surface recombination velocity. The measured *I*–*V* characteristics under the illumination for a representative vertical device are shown in Figure 11a. Fitting the measured photocurrents with Equation (2) yields values of  $\mu_e\tau_e = 1.8 \times 10^{-5} \text{ cm}^2 \text{ V}^{-1}$  and  $\mu_h\tau_h = 0.43 \times 10^{-5} \text{ cm}^2 \text{ V}^{-1}$ .<sup>[88]</sup>

Similarly, as illustrated in Figure 11b, by illuminating the device only near one contact area of a lateral device, depending on the bias voltage polarity, a specific charge carrier type

(hole or electron) can be selected for charge transport in the lateral direction. The measured *I*–*V* characteristics under the illumination for a representative lateral device are shown in Figure 11b. Fitting the measured lateral photocurrents with Equation (2) yields values of  $\mu_e\tau_e = 8.0 \times 10^{-4} \text{ cm}^2 \text{ V}^{-1}$  and  $\mu_h\tau_h = 4.1 \times 10^{-4} \text{ cm}^2 \text{ V}^{-1}$ .<sup>[56]</sup> The measured carrier  $\mu\tau$  products in the lateral direction (*c* plane) are two orders of magnitude larger than those in the vertical direction (*c* axis) for both electrons and holes. The anisotropy transport properties suggest that devices based on *h*-BN should take advantage of its superior lateral transport properties.

#### 4. High-Efficiency Large-Area *h*-BN Neutron Detectors

Neutrons are neutral and interact with matter only weakly, making the direct detection of neutrons quite challenging. However, neutron detectors are vital diagnostic instruments for nuclear and fusion reactor power and safety monitoring, oil field exploration, and neutron imaging and therapy, as well as for plasma and material science research. The development of high-efficiency, compact, and robust semiconductor neutron detectors is expected to dramatically enhance the functionalities of neutron detection systems and open new applications.

The detection of thermal neutrons by a *h*-BN detector is accomplished by a three-step process: 1) the first is the thermal neutron capture by  $^{10}\text{B}$  element in which the nuclear reaction creates Li and  $\alpha$  daughter particles with large kinetic energies; 2) the second process is the subsequent charge carrier (electrons  $[e^-]$  and holes  $[h^+]$ ) generation by energetic Li and  $\alpha$  particles; and 3) the final process of the charge carrier (electrons and holes) separation and collection by the electrodes with the aid of an applied bias voltage or electric field. Therefore, achieving a high efficiency of charge collection is also necessary to ensure an overall high detection efficiency. A high-efficiency *h*-BN thermal neutron detector must have a large-layer thickness according to

Equation (1),  $\eta_i = 1 - e^{-d/\lambda}$ , where  $\lambda$  ( $h^{10}\text{BN}$ ) = 47.3  $\mu\text{m}$ , to ensure a sufficient thermal neutron absorption (high intrinsic efficiency). Moreover, a high-efficiency  $h$ -BN neutron detector must have a recombination time ( $\tau$ ) of the radiation-generated charge carriers that is much greater than the transit time ( $\tau_t$ ),  $\tau \gg \tau_t$ , or equivalently the charge carrier drift length ( $= \mu\tau E$ ) must be greater than the carrier transit distance to ensure a high charge collection efficiency

$$\tau \gg \tau_t, \mu\tau E \gg W \text{ or} \quad (3a)$$

$$\frac{W}{E_{\mu\tau}} = \frac{W^2}{V_{\mu\tau}} < 1, \text{ or } W < \sqrt{V_{\mu\tau}} \quad (3b)$$

where  $W$  is the width (thickness) of a  $h$ -BN lateral (vertical) detectors and  $E$  (V) is the applied electric field (bias voltage).

As demonstrated in Figure 11, the  $\mu\tau$  products in the lateral direction are about 2 orders of magnitude larger than those in the vertical direction. We have developed lateral detector architecture by taking advantage of  $h$ -BN's superior lateral transport properties.<sup>[42,56–58,70–72,75]</sup> The advantages of lateral detectors over vertical detectors can be seen more clearly by using a specific device dimension as an example. For instance, for detectors with the same dimension of 0.2 cm (width,  $W$ )  $\times$  2.0 cm (length,  $L$ )  $\times$  100  $\mu\text{m}$  (thickness,  $d$ ), by fabricating the detector in a lateral geometry, the carrier  $\mu\tau$  products can be enhanced by 2 orders of magnitude, the device capacitance can be reduced by a factor of  $d^2/W^2$  ( $\approx 400$ ), while the surface recombination field can be reduced by a factor of  $(d/W)(\mu_V/\mu_L)$  ( $\approx 2000$ ) and hence can be neglected,<sup>[56]</sup> where  $\mu_L$  and  $\mu_V$  denote the carrier mobilities in the lateral and vertical directions, respectively.

Based on the results shown on Figure 11, the typical lateral  $\mu\tau$  products of these quasi-bulk materials are on the order of  $4 \times 10^{-4} \text{cm}^2 \text{V}^{-1}$ . This means that the detector's width should be designed to be smaller than 4 mm,  $W < 4 \text{mm}$ , for an

operating voltage of 400 V according to Equation (3). As shown schematically in Figure 12a, by combining multiple lateral detectors in parallel, "interdigital finger" type of detectors with large detection areas can be constructed. Each detector strip within the large detector has metal contacts covering the entire vertical edges of the detector of 100  $\mu\text{m}$  in thickness to ensure that the electric field is uniformly applied in the  $c$  plane through the bulk of the detector material, as illustrated in Figure 11b and 12a. An optical image of a finished 1  $\text{cm}^2$  detector fabricated from a  $h^{10}\text{BN}$  quasi-bulk wafer (100  $\mu\text{m}$  thick) by combining 6 detector lateral strips fabricated is shown in the bottom panel of Figure 12a.

A Californium-252 ( $^{252}\text{Cf}$ ) source was used as a neutron source. A cube made of high-density polyethylene (HDPE) is used to moderate the fast neutrons via elastic scattering between neutrons and hydrogen atoms inside HDPE. The fast neutrons from the  $^{252}\text{Cf}$  source will be thermalized through the process of losing their energies by elastic scattering with hydrogen atoms. When the  $^{252}\text{Cf}$  source is placed at the center location of the HDPE moderator, the probability of neutron emission reaching outside of the HDPE block is nearly zero. When the  $^{252}\text{Cf}$  source is placed at 2.5 cm from the front surface of the HDPE block, a maximum flux of thermal neutrons is obtained.<sup>[52–57,72]</sup> Detection electronics consist of a charge sensitive preamplifier, shape shaping amplifier, and multichannel analyzer.

The thermal neutron detection efficiencies were measured by placing the detectors at 30 cm from the HDPE block front face and side by side with a  $^6\text{LiF}$ -filled microstructured semiconductor neutron detector (MSND) with a known detection area (4  $\text{cm}^2$ ) and detection efficiency (30%). By measuring the counts against this MSND detector, the detection efficiencies of  $h^{10}\text{BN}$  detectors can be obtained. The sensitivity of  $h^{10}\text{BN}$  to  $\gamma$  photons was tested by measuring the pulsed height spectra (PHS) of  $h^{10}\text{BN}$  detector in the presence of a 662 keV  $^{137}\text{Cs}$  source and the results indicated that the sensitivity of  $h^{10}\text{BN}$  detectors to

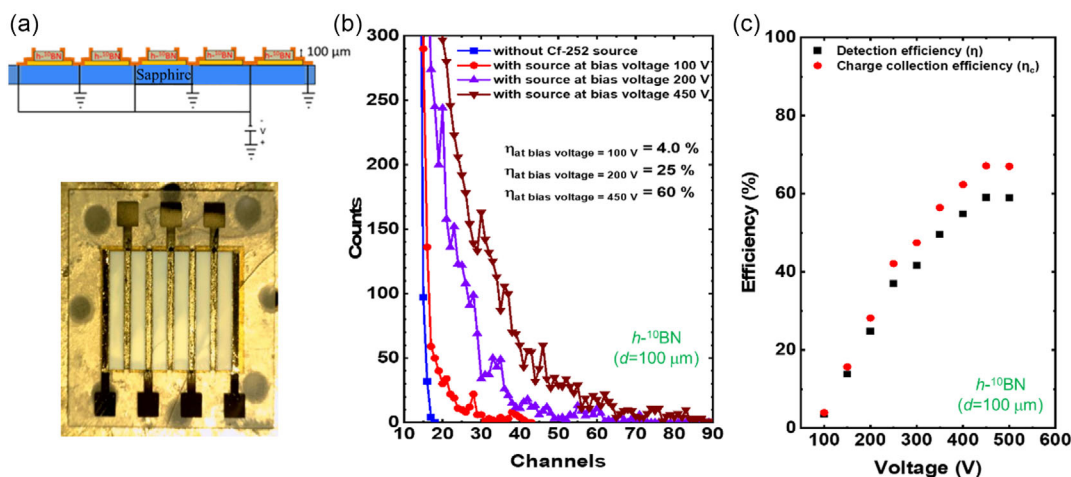


**Figure 12.** a) Schematic of connecting multiple  $h$ -BN lateral detector strips in parallel to form a large area detector. b) Optical image of a finished 1  $\text{cm}^2$  thermal neutron detector formed by connecting in parallel six detector strips fabricated from a 100  $\mu\text{m}$  thick  $h^{10}\text{BN}$  wafer. (b) Pulse height spectra (PHS) measured at three different voltages. The blue curve is the background (or dark) counts measured at the same bias voltage. c) Plot of the measured detection efficiency ( $\eta$ ) and effective charge collection efficiency ( $\eta_c$ ) as functions of the applied voltage. Reproduced under terms of the CC-BY license.<sup>[72]</sup> Copyright 2024, The Authors.

$\gamma$  photons from 662 keV  $^{137}\text{Cs}$  source is at the background level.<sup>[42,57,72]</sup> This is because BN is composed of low atomic elements B and N. By setting the lower-level discrimination in the detection electronics corresponding to the response of the detector to 662 keV  $^{137}\text{Cs}$   $\gamma$  photons, any response to  $\gamma$  photons can successfully filtered out.

Figure 12b shows the PHS of a 1 cm<sup>2</sup> lateral detector fabricated from a 100  $\mu\text{m}$  thick  $h$ - $^{10}\text{BN}$  wafer, measured at several bias voltages. The measured detector efficiency ( $\eta$ ) as a function of the applied voltage (and electric field) is plotted in Figure 12c, which shows that at a bias voltage of 450 V, this 1 cm<sup>2</sup> detector delivers a record high detection efficiency for thermal neutrons of 60%,<sup>[72]</sup> although a 3.6 eV emission band is observed in most HVPE wafers produced to date. By defining the charge collection efficiency ( $\eta_c$ ) as the ratio of measured efficiency to theoretical efficiency of  $\eta_i = 1 - e^{-d/\lambda}$ , Figure 12c also plots  $\eta_c$  as a function of the applied voltage, yielding a maximum collection efficiency of 68%. The value of  $\eta_c$  is also a good measure of  $h$ -BN material quality, whereas the ideal value of  $\eta_c$  is 100%. We anticipate a significant improvement in the  $\mu\tau$  product if we can minimize the density of native defects through monitoring and eliminating the 3.6 eV emission band. This would further boost  $\eta_c$  and facilitate the fabrication of large-area detectors with greater ease. The feasibility of  $h$ -BN for fast neutrons detection has also been demonstrated.<sup>[58,75]</sup> Identification of a single material that is sensitive to both thermal and fast neutrons is valuable for the development of novel neutron detection technologies.

## 5. Potential as an Outstanding Electronic Material

Using the experimentally measured breakdown field value of bulk  $h$ -BN of  $E_C = 12 \text{ MV cm}^{-1}$  (Figure 3),<sup>[29]</sup> thermal conductivity of  $\kappa = 550 \text{ W m}^{-1} \text{ K}^{-1}$  (Figure 4),<sup>[30]</sup> dielectric constant of 5,<sup>[50]</sup> and electron mobility of  $\mu = 120 \text{ cm}^2 \text{ V}^{-1} \text{ s}^{-1}$ ,<sup>[89]</sup> the calculated Baliga's figure of merit ( $\text{BFOM} = \epsilon \cdot \mu_e \cdot E_C^3$ ) of  $h$ -BN with respect to Si exceeds 3000, making  $h$ -BN an attractive electronic material. This is expected based on the established relationship between  $E_C$  and  $E_g$  of  $E_C \approx E_g^{1.86}$ .<sup>[90]</sup> However, the ability of doping and conductivity control of  $h$ -BN appear to be very poor because the energy levels of all known impurities in  $h$ -BN are larger than

0.5 eV.<sup>[91,92]</sup> These properties together make a strong case for utilizing  $h$ -BN as one of the materials of choice for light-triggered electronic power switches known as photoconductive semiconductor switches (PCSS).<sup>[93]</sup>

Compared to traditional power switches, PCSS devices exhibit distinctive features, including reliable ultrafast operation at high voltages and currents, optical coupling of control circuits that are electrically isolated from the switched high voltage, compact design, negligible jitter time, and low inductance.<sup>[94–98]</sup> However, existing PCSS devices are incapable of meeting the simultaneous demands of high hold-off voltage, high on-state current, high frequency, and compactness. Although the introduction of extrinsic PCSS devices based on GaN and SiC WBG semiconductors has enhanced either operating voltage or current, it has been challenging to achieve improvements in both areas simultaneously. This limitation arises because WBG PCSS devices require the use of semi-insulating materials. These materials are created by doping with deep-level acceptors to trap electrons from both intentional and unintentional shallow donors, as depicted in Figure 13a. These trapped electrons can then be optically excited from the deep-level acceptors into the conduction band, facilitating the transition of GaN or SiC materials from a semi-insulating (off) state to a conducting (on) state. However, this method cannot effectively support both high hold-off voltage and high photocurrent at the same time. The total impurity concentration (comprising shallow donors and deep acceptors) is often too high to allow for effective high-voltage operation. Conversely, the number of optically active compensated acceptors tends to be insufficient to sustain high photocurrent operation. Additionally, electron mobility is significantly influenced by compensation doping, as both donors and compensating acceptors become ionized. More importantly, the critical fields of GaN and SiC are about 4 times lower than that of  $h$ -BN.

As shown in Figure 13b, existing experimental and theoretical data indicate that Si substitutes on the B site, forming a donor level situated 1.2 eV below the CBM in  $h$ -BN.<sup>[92,99]</sup> This donor level is sufficiently deep to facilitate an extremely low leakage current. A significant advantage of extrinsic PCSS over intrinsic PCSS is their capacity to support a large optical absorption length. This characteristic allows for the conduction throughout

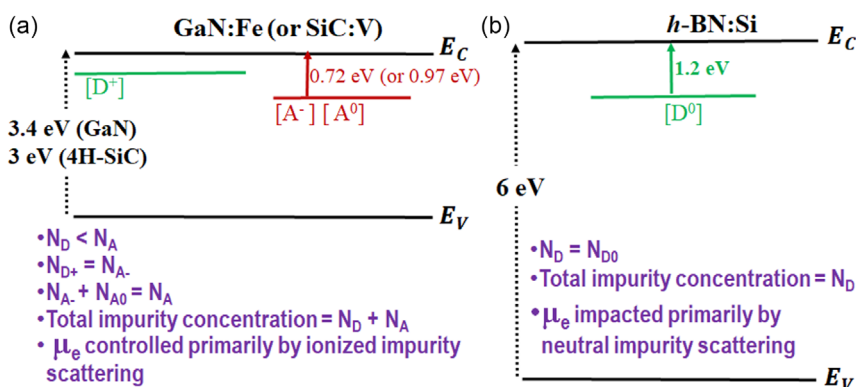


**Figure 13.** Energy diagram illustrating excitation mechanisms of PCSS operation in a) Fe compensation doped GaN (or V compensation doped 4H-SiC) and b) Si-doped  $h$ -BN.

the bulk of the devices, thereby enabling high-voltage and high-power operation. However, achieving this capability necessitates the development of large-diameter, high-quality *h*-BN quasi-bulk crystals.

## 6. Concluding Remarks

We provided a brief overview of the current status of *h*-BN quasi-bulk crystal development. Structural characterization results indicate that *h*-BN quasi-bulk wafers, with a thickness of 100  $\mu\text{m}$ , exhibit a well-defined stacking sequence and long-range order along the *c* axis. Due to the layered crystalline structure of *h*-BN, many of its physical properties are anisotropic. Notably, the measured mobility-lifetime products in the lateral direction (within the *c* plane) are  $\approx 2$  orders of magnitude greater than those measured in the vertical direction (along the *c* axis) for both electrons and holes. Lateral thermal neutron detectors with a detection area of 1  $\text{cm}^2$ , fabricated from 100  $\mu\text{m}$  thick *h*-<sup>10</sup>BN wafers, have demonstrated a record-high detection efficiency of 60% at a bias voltage of 450 V. Given its unique physical properties, *h*-BN shows promise for applications in PCSS devices capable of supporting high-voltage and high-power operations. Additionally, *h*-BN has been recognized as a promising UWBG material for various applications, including deep ultraviolet photonics, substrates for 2D devices, hyperbolic dispersion devices, and solid-state hosts for single-photon emitters and quantum qubits. These applications would greatly benefit from the availability of high-quality, large-diameter quasi-bulk crystals. Consequently, the ability to produce large-diameter *h*-BN quasi-bulk materials, whether as active media or substrates, is becoming increasingly important.

## Acknowledgements

The efforts of *h*-BN quasi-bulk crystal growth by HVPE and high-efficiency neutron detector developments were funded in part by the Advanced Research Projects Agency-Energy (ARPA-E), U.S. Department of Energy, grant nos. DE-AR0001552, DE-AR0001257, DE-AR000964, and DE-AR0001821, monitored by Dr. Olga Spahn, Dr. Isik Kizilyalli, and Dr. Eric Carlson. The views and opinions of authors expressed herein do not necessarily state or reflect those of the United States Government or any agency thereof. The authors are grateful to the AT&T Foundation for the support of Ed Whitacre and Linda Whitacre endowed chairs.

## Conflict of Interest

The authors declare no conflict of interest.

## Keywords

defects in semiconductors, epitaxial growths, *h*-BNs, hexagonal boron nitrides (*h*-BNs), neutron detectors, quasi-bulk crystals, ultrawide bandgap (UWBG) semiconductors

Received: November 10, 2024

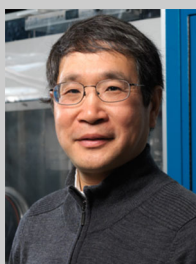
Revised: April 18, 2025

Published online:

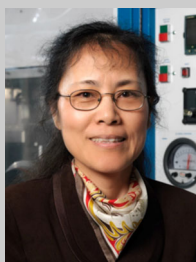
- [1] The Royal Swedish Academy of Sciences has decided to award the Nobel Prize in Physics for 2014 to Isamu Akasaki, Hiroshi Amano, and Shuji Nakamura “for the invention of efficient blue light-emitting diodes which has enabled bright and energy-saving white light sources,” (accessed Nov. 2024) <https://www.nobelprize.org/prizes/physics/2014/press-release>.
- [2] S. Pimputkar, J. S. Speck, S. P. DenBaars, S. Nakamura, *Nat. Photonics* **2009**, 3, 180.
- [3] H. Amano, N. Sawaki, I. Akasaki, Y. Toyoda, *Appl. Phys. Lett.* **1986**, 48, 353.
- [4] S. Nakamura, T. Mukai, M. Senoh, *Appl. Phys. Lett.* **1994**, 64, 1687.
- [5] M. A. Khan, R. A. Skogman, R. G. Schulze, M. Gershenson, *Appl. Phys. Lett.* **1983**, 42, 430.
- [6] M. Asif Khan, A. Bhattarai, J. N. Kuznia, D. T. Olson, *Appl. Phys. Lett.* **1993**, 63, 1214.
- [7] H. Amano, Y. Baines, E. Beam, Matteo Borga, T Bouchet, Paul R Chalker, M Charles, Kevin J Chen, Nadim Chowdhury, Rongming Chu, Carlo De Santi, Maria Merlyne De Souza, Stefaan Decoutere, L Di Cioccio, Bernd Eckardt, Takashi Egawa, P Fay, Joseph J Freedsmann, L Guido, Oliver Häberlen, Geoff Haynes, Thomas Heckel, Dilini Hemakumara, Peter Houston, Jie Hu, Mengyuan Hua, Qingyun Huang, Alex Huang, Sheng Jiang, H Kawai, Dan Kin-zer, Martin Kuball, J. Phys. D: Appl. Phys. **2018**, 51, 163001.
- [8] Y. H. Chen, J. Encomendero, C. Savant, V. Protasenko, H. G. Xing, D. Jena, *Appl. Phys. Lett.* **2024**, 124, 152111.
- [9] J. Y. Tsao, S. Chowdhury, M. A. Hollis, D. Jena, N. M. Johnson, K. A. Jones, R. J. Kaplar, S. Rajan, C. G. Van de Walle, E. Bellotti, C. L. Chua, R. Collazo, M. E. Coltrin, J. A. Cooper, K. R. Evans, S. Graham, T. A. Grotjohn, E. R. Heller, M. Higashiwaki, M. S. Islam, P. W. Juodawlkis, M. A. Khan, A. D. Koehler, J. H. Leach, U. K. Mishra, R. J. Nemanich, R. C. N. Pilawa-Podgurski, J. B. Shealy, Z. Sitar, M. J. Tadjer, A. F. Witulski, M. Wraback, J. A. Simmons *Adv. Electron. Mater.* **2018**, 4, 1600501.
- [10] S. X. Jin, J. Li, J. Z. Li, J. Y. Lin, H. X. Jiang, *Appl. Phys. Lett.* **2000**, 76, 631.
- [11] H. X. Jiang, S. X. Jin, J. Li, J. Shakya, J. Y. Lin, *Appl. Phys. Lett.* **2001**, 78, 1303.
- [12] J. Day, J. Li, D. Y. C. Lie, C. Bradford, J. Y. Lin, H. X. Jiang, *Appl. Phys. Lett.* **2011**, 99, 031116.
- [13] J. Y. Lin, H. X. Jiang, *Appl. Phys. Lett.* **2020**, 116, 100502.
- [14] H. X. Jiang, J. Y. Lin, *Nat. Electron.* **2023**, 6, 257.
- [15] P. J. Parbrook, B. Corbett, J. Han, T. Y. Seong, H. Amano, *Laser Photonics Rev.* **2021**, 15, 2000133.
- [16] J. Wu, W. Walukiewicz, K. Yu, J. W. Ager III, E. E. Haller, H. Lu, W. J. Schaff, Y. Saito, Y. Nanishi, *Appl. Phys. Lett.* **2002**, 80, 4741.
- [17] S. Vanka, B. Zhou, R. A. Awni, Z. Song, F. A. Chowdhury, X. Liu, H. Hajibabaei, W. Shi, Y. Xiao, I. A. Navid, A. Pandey, R. Chen, G. A. Botton, T. W. Hamann, D. Wang, Y. Yan, Z. Mi, *ACS Energy Lett.* **2020**, 5, 3741.
- [18] M. A. Khan, K. Balakrishnan, T. Katona, *Nat. Photonics* **2008**, 2, 77.
- [19] Z. Zhang, M. Kushimoto, T. Sakai, N. Sugiyama, L. J. Schowalter, C. Sasaoka, H. Amano, *Appl. Phys. Express* **2019**, 12, 124003.
- [20] N. K. Hossain, A. Tingsuwatit, Z. Alemoush, M. Almohammad, J. Li, J. Y. Lin, H. X. Jiang, *Appl. Phys. Express* **2024**, 17, 091001.
- [21] A. K. Geim, I. V. Grigorieva, *Nature* **2013**, 499, 419.
- [22] R. Bourrellier, S. Meuret, A. Tararan, O. Stephan, M. Kociak, L. H. G. Tizei, A. Zobelli, *Nano Lett.* **2016**, 16, 4317.
- [23] T. Sugino, K. Tanioka, S. Kawasaki, J. Shirafuji, *Jpn. J. Appl. Phys.* **1997**, 36, L463.
- [24] K. Watanabe, T. Taniguchi, H. Kanda, *Nat. Mater.* **2004**, 3, 404.

- [25] B. Arnaud, S. Lebégue, P. Rabiller, M. Alouani, *Phys. Rev. Lett.* **2006**, 96, 026402.
- [26] Y. Kubota, K. Watanabe, O. Tsuda, T. Taniguchi, *Science* **2007**, 317, 932.
- [27] G. Cassaboïs, P. Valvin, B. Gil, *Nat. Photonics* **2016**, 10, 262.
- [28] Y. Hattori, T. Taniguchi, K. Watanabe, K. Nagashio, *ACS Appl. Mater. Interfaces* **2016**, 8, 27877.
- [29] Y. Hattori, T. Taniguchi, K. Watanabe, K. Nagashio, *Appl. Phys. Lett.* **2016**, 109, 253111.
- [30] C. Yuan, J. Li, L. Lindsay, D. Cherns, J. W. Pomeroy, S. Liu, J. H. Edgar, M. Kuball, *Commun. Phys.* **2019**, 2, 43.
- [31] O. Osberghaus, *Z. Phys.* **1950**, 128, 366.
- [32] G. F. Knoll, *Radiation Detection and Measurement*, 4th ed., John Wiley & Sons **2010**.
- [33] Y. Kumagai, T. Yamane, A. Koukitu, *J. Cryst. Growth* **2005**, 281, 62.
- [34] Y. Kumagai, K. Goto, T. Nagashima, R. Yamamoto, M. Bockowski, J. Kotani, *Appl. Phys. Express* **2022**, 15, 115501.
- [35] L. Wirtz, A. Marini, A. Rubio, *Phys. Rev. Lett.* **2006**, 96, 126104.
- [36] L. Wirtz, A. Marini, M. Gruning, C. Attaccalite, G. Kresse, A. Rubio, *Phys. Rev. Lett.* **2008**, 100, 189701.
- [37] J. Serrano, A. Bosak, R. Arenal, M. Krisch, K. Watanabe, T. Taniguchi, H. Kanda, A. Rubio, L. Wirtz, *Phys. Rev. Lett.* **2007**, 98, 095503.
- [38] L. Artús, M. Feneberg, C. Attaccalite, J. H. Edgar, J. Li, R. Goldhahn, *Adv. Photonics Res.* **2021**, 2, 2000101.
- [39] J. Li, K. B. Nam, M. L. Nakarmi, J. Y. Lin, H. X. Jiang, P. Carrier, S.-H. Wei, *Appl. Phys. Lett.* **2003**, 83, 5163.
- [40] T. Q. P. Vuong, G. Cassaboïs, P. Valvin, V. Jacques, A. Van Der Lee, A. Zobelli, K. Watanabe, T. Taniguchi, B. Gil, *2D Mater.* **2017**, 4, 011004.
- [41] S. F. Chichibu, K. Shima, K. Kikuchi, N. Umehara, K. Takiguchi, Y. Ishitani, K. Hara, *Appl. Phys. Lett.* **2022**, 120, 231904.
- [42] A. Maity, S. J. Grenadier, J. Li, J. Y. Lin, H. X. Jiang, *Prog. Quantum Electron.* **2021**, 76, 100302.
- [43] S. Majety, X. K. Cao, J. Li, R. Dahal, J. Y. Lin, H. X. Jiang, *Appl. Phys. Lett.* **2012**, 101, 051110.
- [44] B. Huang, X. K. Cao, H. X. Jiang, J. Y. Lin, S. H. Wei, *Phys. Rev. B* **2012**, 86, 155202.
- [45] J. Li, S. Majety, R. Dahal, W. P. Zhao, J. Y. Lin, H. X. Jiang, *Appl. Phys. Lett.* **2012**, 101, 171112.
- [46] R. R. Nair, P. Blake, A. N. Grigorenko, K. S. Novoselov, T. J. Booth, T. Stauber, N. M. R. Peres, A. K. Geim, *Science* **2008**, 320, 1308.
- [47] K. B. Nam, J. Li, M. L. Nakarmi, J. Y. Lin, H. X. Jiang, *Appl. Phys. Lett.* **2004**, 84, 5264.
- [48] A. Ranjan, Sean J. O'Shea, Andrea Padovani, Tong Su, Paolo La Torraca, Yee Sin Ang, Manveer Singh Munde, Chenhui Zhang, Xixiang Zhang, Michel Bosman, Nagarajan Raghavan, and Kin Leong Pey et al., *ACS Appl. Electron. Mater.* **2021**, 3, 3547.
- [49] M. A. McKay, J. Li, J. Y. Lin, H. X. Jiang, *J. Appl. Phys.* **2020**, 127, 0531032.
- [50] R. Geick, C. H. Perry, G. Rupprecht, *Phys. Rev.* **1966**, 146, 543.
- [51] J. Li, R. Dahal, S. Majety, J. Y. Lin, H. X. Jiang, *Nucl. Instrum. Methods Phys. Res., Sect. A* **2011**, 654, 417.
- [52] T. C. Doan, S. Majety, S. Grenadier, J. Li, J. Y. Lin, H. X. Jiang, *Nucl. Instrum. Methods Phys. Res., Sect. A* **2014**, 748, 84.
- [53] K. Ahmed, R. Dahal, A. Weltz, J.-Q. Lu, Y. Danon, I. B. Bhat, *Appl. Phys. Lett.* **2016**, 109, 113501.
- [54] A. Maity, T. C. Doan, J. Li, J. Y. Lin, H. X. Jiang, *Appl. Phys. Lett.* **2016**, 109, 072101.
- [55] A. Maity, S. J. Grenadier, J. Li, J. Y. Lin, H. X. Jiang, *Appl. Phys. Lett.* **2017**, 111, 033507.
- [56] A. Maity, S. J. Grenadier, J. Li, J. Y. Lin, H. X. Jiang, *Appl. Phys. Lett.* **2019**, 114, 222102.
- [57] A. Maity, S. J. Grenadier, J. Li, J. Y. Lin, H. X. Jiang, *Appl. Phys. Lett.* **2020**, 116, 142102.
- [58] A. Tingsuwatit, A. Maity, S. J. Grenadier, J. Li, J. Y. Lin, H. X. Jiang, *Appl. Phys. Lett.* **2022**, 120, 232103.
- [59] T. Taniguchi, K. Watanabe, *J. Cryst. Growth* **2007**, 303, 525.
- [60] N. D. Zhigadlo, *J. Cryst. Growth* **2014**, 402, 308.
- [61] Y. Li, V. Garnier, P. Steyer, C. Journet, B. Toury, *ACS Appl. Nano Mater.* **2020**, 3, 1508.
- [62] J. Li, J. Wang, X. Zhang, C. Elias, G. Ye, D. Evans, G. Eda, J. M. Redwing, G. Cassaboïs, B. Gil, P. Valvin, R. He, B. Liu, J. H. Edgar, *Chem. Mater.* **2020**, 32, 5066.
- [63] T. S. Cheng, A. Summerfield, C. J. Mellor, A. Davies, A. N. Khlobystov, L. Eaves, C. T. Foxon, P. H. Beton, S. V. Novikov, *J. Vac. Sci. Technol., B: Nanotechnol. Microelectron.: Mater., Process., Meas., Phenom.* **2018**, 36, 02D103.
- [64] D. A. Laleyan, K. Mengle, S. Zhao, Y. Wang, E. Kioupakis, Z. Mi, *Opt. Express* **2018**, 26, 23031.
- [65] Z. Xu, H. Tian, A. Khanaki, R. Zheng, M. Suja, J. Liu, *Sci. Rep.* **2017**, 7, 43100.
- [66] P. Vuong, T. Moudakir, R. Gujrati, A. Srivastava, V. Ottapilakkal, S. Gautier, P. L. Voss, S. Sundaram, J. P. Salvestrini, A. Ougazzaden, *Adv. Mater. Technol.* **2023**, 8, 2300600.
- [67] E. A. Preble, J. H. Leach, R. Metzger, E. Shishkin, K. A. Udwaray, *Phys. Status Solidi C* **2014**, 11, 604.
- [68] S. Kaneki, T. Konno, T. Kimura, K. Kanegae, J. Suda, H. Fujikura, *Appl. Phys. Lett.* **2024**, 124, 012105.
- [69] K. Ohnishi, N. Fujimoto, S. Nitta, H. Watanabe, S. Lu, M. Deki, Y. Honda, H. Amano, *J. Appl. Phys.* **2022**, 132, 145703.
- [70] Z. Alemoush, N. K. Hossain, A. Tingsuwatit, M. Almohammad, J. Li, J. Y. Lin, H. X. Jiang, *Appl. Phys. Lett.* **2023**, 122, 012105.
- [71] Z. Alemoush, A. Tingsuwatit, J. Li, J. Y. Lin, H. X. Jiang, *Crystals* **2023**, 13, 1319.
- [72] Z. Alemoush, A. Tingsuwatit, A. Maity, J. Li, J. Y. Lin, H. X. Jiang, *J. Appl. Phys.* **2024**, 135, 175704.
- [73] R. Cuscó, L. Artús, J. H. Edgar, S. Liu, G. Cassaboïs, B. Gil, *Phys. Rev. B* **2018**, 97, 155435.
- [74] B. N. Pantha, R. Dahal, M. L. Nakarmi, N. Nepal, J. Li, J. Y. Lin, H. X. Jiang, Q. S. Paduano, David Weyburne, *Appl. Phys. Lett.* **2007**, 90, 241101.
- [75] J. Li, A. Tingsuwatit, Z. Alemoush, J. Y. Lin, H. X. Jiang, *APL Mater.* **2025**, 13, 011101.
- [76] J. Li, J. Y. Lin, H. X. Jiang, *APL Mater.* **2024**, 12, 111115.
- [77] J. Li, X. K. Cao, T. B. Hoffman, J. H. Edgar, J. Y. Lin, H. X. Jiang, *Appl. Phys. Lett.* **2016**, 108, 122101.
- [78] K. Watanabe, T. Taniguchi, *Phys. Rev. B* **2009**, 79, 193104.
- [79] K. Watanabe, T. Taniguchi, T. Kuroda, O. Tsuda, H. Kanda, *Diamond Relat. Mater.* **2008**, 17, 830.
- [80] X. K. Cao, B. Clubine, J. H. Edgar, J. Y. Lin, H. X. Jiang, *Appl. Phys. Lett.* **2013**, 103, 191106.
- [81] M. Almohammad, Z. Alemoush, J. Li, J. Y. Lin, H. X. Jiang, *Appl. Phys. Lett.* **2024**, 124, 102106.
- [82] N. Nepal, M. L. Nakarmi, J. Y. Lin, H. X. Jiang, *Appl. Phys. Lett.* **2006**, 89, 092107.
- [83] K. B. Nam, M. L. Nakarmi, J. Y. Lin, H. X. Jiang, *Appl. Phys. Lett.* **2005**, 86, 222108.
- [84] A. Many, *J. Phys. Chem. Solids* **1965**, 26, 575.
- [85] U. Lachish, *Nucl. Instrum. Methods Phys. Res., Sect. A* **1998**, 403, 417.
- [86] N. Beck, N. Wyrtsch, Ch Hof, *J. Appl. Phys.* **1996**, 79, 9361.
- [87] Š. Uxa, R. Grill, *J. Appl. Phys.* **2013**, 114, 094511.
- [88] S. J. Grenadier, A. Maity, J. Li, J. Y. Lin, H. X. Jiang, *Appl. Phys. Lett.* **2018**, 112, 162103.
- [89] M. M. Khatami, M. L. Van de Put, W. G. Vandenberghe, *Phys. Rev. B* **2021**, 104, 235424.

- [90] O. Slobodyan, J. Flicker, J. Dickerson, J. Shoemaker, A. Binder, T. Smith, S. Goodnick, R. Kaplar, M. Hollis, *J. Mater. Res.* **2022**, 37, 849.
- [91] L. Weston, D. Wickramaratne, M. Mackoite, A. Alkauskas, C. G. Van de Walle, *Phys. Rev. B* **2018**, 97, 214104.
- [92] F. Oba, A. Togo, I. Tanaka, K. Watanabe, T. Taniguchi, *Phys. Rev. B* **2010**, 81, 075125.
- [93] ARPA-E - Department of Energy - The Unlocking Lasting Transformative Resiliency Advances by Faster Actuation of Power Semiconductor Technologies (ULTRAFast) program - Ultrawide bandgap semiconductors for extrinsic photoconductive switching devices.
- [94] J. S. Sullivan, <https://doi.org/10.2172/1034509>.
- [95] S. E. Sampayan, P. V. Grivickas, A. M. Conway, K. C. Sampayan, I. Booker, M. Bora, G. J. Caporaso, V. Grivickas, H. T. Nguyen, K. Redeckas, A. Schoner, L. F. Voss, M. Vengris and L. Wang, *Sci. Rep.* **2021**, 11, 6859.
- [96] K. Zhu, S. Dogan, Y. T. Moon, J. Leach, F. Yun, D. Johnstone, H. Morkoç, G. Li, B. Ganguly, *Appl. Phys. Lett.* **2005**, 86, 2561108.
- [97] J. H. Leach, R. Metzger, E. Preble, K. R. Evans, *Proc. SPIE* **2013**, 8625, 86251Z.
- [98] E. Majda-Zdancewicz, M. Suproniuk, M. Pawłowski, M. Wierzbowski, *Opto-Electron. Rev.* **2018**, 26, 92.
- [99] S. Majety, T. C. Doan, J. Li, J. Y. Lin, H. X. Jiang, *AIP Adv.* **2013**, 3, 122116.



**Hongxing Jiang** received his Ph.D. in physics from Syracuse University. He invented microLED and microLED microdisplay in 2000, propelling the microLED display industry. He is the Ed Whitacre Endowed Chair and Horn Distinguished Professor of ECE at Texas Tech University (TTU). He relocated his group to TTU in 2008 from Kansas State University where he was a University Distinguished Professor. He is an elected fellow of the AAAS, APS, Optica, SPIE, and NAI. He was awarded the “Global SSL Award of Outstanding Achievements” in 2021 for his invention of microLED by the International SSL Alliance.



**Jingyu Lin** is the Linda F. Whitacre Endowed Chair and Horn Distinguished Professor of ECE at Texas Tech University. She is a co-inventor microLED technology, leading to the realization of microLED displays and single-chip AC-LEDs. She is an elected fellow of the AAAS, APS, Optica, SPIE, and NAI for her pioneering contributions to epitaxial growth, fundamental understanding, and practical applications of III-nitride wide bandgap semiconductors. She earned her Ph.D. from Syracuse University. She relocated to TTU in 2008 from Kansas State University where she was a professor of physics.